Research on Dielectric-Loaded Surface Plasmon Polariton Waveguides

Hyunjun Lim

Department of Electrical Engineering

Graduate school of UNIST

Research on Dielectric-Loaded Surface Plasmon Polariton Waveguides

A thesis
Submitted to the Graduate School of UNIST
in partial fulfillment of the
requirements for the degree of
Master of Science

Hyunjun Lim

01. 29. 2014 of submission
Approved by

Major Advisor
Min Suk Kwon

Research on Dielectric-Loaded Surface Plasmon Polariton Waveguides

Hyunjun Lim

This certifies that the thesis of Hyunjun Lim is approved.

01. 29. 2014 of submission

Signature

Thesis Supervisor: Min Suk Kwon

Signature

Kibog Park: Thesis Committee Member #1

Signature

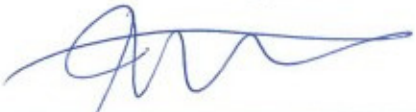

Min Sup Hur: Thesis Committee Member #2

Abstract

Surface plasmon polaritons (SPPs) are electromagnetic waves which propagate along metal-dielectric interfaces. SPPs can overcome the diffraction limit, and they have received a lot of interest due to strong confinement of energy. Therefore, a variety of nanoplasmonic waveguides based on SPPs have been investigated. Dielectric-loaded surface plasmon polariton (DLSPP) waveguides are a representative example of nanoplasmonic waveguides. In this thesis, improvement of two characteristics of a DLSPP waveguide is studied, and realization of DLSPP waveguides is investigated. First, the efficiency of coupling between a DLSPP waveguide and a photonic waveguide is improved. For this purpose, the use of a dielectric with a higher refractive index than the previously used dielectric in [Opt. Express **18**, 5314 (2010)] is proposed. The loss of the coupling between the photonic and DLSPP waveguides based on a dielectric of refractive index 1.57 is reduced to 2.3 dB, and the coupling is achieved through a 3-μm-long coupling region. The coupling loss is further reduced by modifying the DLSPP waveguide into a double-dielectric-loaded surface plasmon polariton (D^2LSPP) waveguide. The D^2LSPP waveguide can be coupled to the photonic waveguide with a coupling loss of 1.1 dB through a 4-μm-long coupling region. Moreover, almost only the fundamental transverse-magnetic mode of the D^2LSPP waveguide is excited after the short coupling region. The coupling loss is about a third of that in the reference, and the coupling region length is about one order of magnitude smaller than that in the reference. Second, bends of DLSPP waveguides are improved. For this purpose, 60º fan-shaped bends of DLSPP waveguides are proposed. By reducing a bending angle from 90° to 60° and introducing a fan-shaped structure, the bending radius of the 60º fan-shaped bend is reduced to 2 μm, and its bending loss is just 0.76 dB. Finally, a fabrication process of DLSPP waveguide based on the commercially available photoresist SU8 is developed. The process consists of optical lithography, a lift-off step, e-beam lithography, etc. The characteristics of the fabricated DLSPP waveguides are discussed. Based on the DLSPP or D^2LSPP waveguides and the 60º fan-shaped bends, which are investigated in this work, a highly-integrated planar lightwave circuit with a relatively low loss may be developed.

Contents

List of Figures

Figure 2-7. (a) Cross-sectional structure of the D^2LSPP waveguide. (b) Intensity profile of the fundamental TM mode TM_{d00} of the D^2LSPP waveguide for h_d = 0.6 μm, h_d' = 0.4 μm, and n_d' = 1.45.

Figure 2-8. (a) Relations of the effective mode area and propagation loss of TM_{d00} to h_d'. (b), (c), and (d) show the distributions of the magnitude of the *y*-component of the electric field of TM_{d00}, $|E_y|$, along the vertical centerline of the loaded dielectric for h_d' = 0.2, 0.4 and 0.8 μm, respectively.

Figure 2-9. Relation of the coupling loss to h_d'. The circle symbols are obtained from the calculation based on the FDTD method. The red solid line is a guide for the eyes.

Figure 2-10. Transmittance at P_3 vs. l_d. The circle symbols are obtained from the calculation based on the FDTD method. The solid straight line has a slope equal to $-\alpha_d$, and they pass the calculated transmittance at l_d = 30 μm. The inset shows the distributions of the magnitude of the magnetic field at P_2.

Figure 3-1. Relations of the transmission to the bend radius R of the 90º curved bend [32].

Figure 3-2. (a) Cross-sectional structure of the DLSPP waveguide. (b) 60º curved bend of the DLSPP waveguide. (c) Proposed 60º fan-shaped bend of the DLSPP waveguide.

Figure 3-3. Relations of the transmission to the bend radius R of the 90º curved bend, 60º curved bend and 60º fan-shaped curved bend.

Figure 3-4. Distributions of the magnitude of the z-component of the electric field of 60º fan-shaped curved bend of the DLSPP waveguide. (a) R = 0.75 μm. (b) R = 2.5 μm.

Figure 4-1. Fabrication process of DLSPP waveguide (1).

Figure 4-2. Fabrication process of DLSPP waveguide (2).

Figure 4-3. Surface SEM images of the waveguide pattern. (a) Sample #1 (b) Sample #2 (c) Sample #3 (d) Sample #4.

Figure 4-4. (a) Surface SEM image of the fabricated DLSPP waveguide. (b) The cross-section image of the SU8 pattern. The SU8 pattern was covered by Pt in order to form the cross-section by using focused ion beam milling.

List of Tables

Nomenclature

SPPs	Surface plasmon polaritons
DLSPP	Dielectric loaded surface plasmon polariton
D^2LSPP	Double dielectric loaded surface plasmon polariton
TM	Transverse-magnetic
TE	Transverse-electric
MIM	Metal-insulator-metal
MISIM	Metal-insulator-silicon-insulator-metal
SEM	Scanning electron microscope
PMMA	Poly methyl methacrylate
FDTD	Finite difference time domain
HSQ	hydrogen silsesquioxane
PR	Photo resist
UV	Ultra violet
RIE	Reactive ion etching

Chapter 1

Introduction

In the 20th century, telecommunications market experienced spectacular growth, with the explosion of the internet. As the result of the growth, optical communications was also very successful. In modern society, optical techniques are used in the fields of all the kinds of communications. Hence, it is necessary to develop optical and optoelectronic components with a planar technology, which are able to generate, detect modulate or commutate light, using waveguide structures. This field of research is called for integrated optics.

The concept of "integrated optics" was introduced for the first time by S.E. Miller in 1960. The approach suggested by Miller is to create on the same substrate, passive and active components for light generation and treatment. The basic element of this type of circuit is an optical waveguide.

The physicist R. Feynman suggested for the first time the concept of "Smaller, Faster, Cheaper", which is handling matter on an atomic and molecular scale in order to conceive and produce sub-micrometric components and systems. Following this concept, the concept of nanotechnology, which became a new challenge for scientific research, appeared. Based on this new paradigm, nano-photonics makes it possible to develop new optical components for light generation and treatment. However, when integrated-optical circuits are realized, there is a physical limit on miniaturization because of the nature of light. It is important in achieving the performance of the integrated circuit to optimize the functions of the elements constituting an integrated-optical circuit. Therefore, hybrid integration technologies have emerged. Hybrid integrated circuit techniques are basically based on a combination of devices made up of different materials. Thus, individual devices and substrates require optimization of coupling between different devices. Compared to monolithic integration techniques using the same material, hybrid integration technique has advantages of reduced technical difficulty and rather high yield. In addition, it can pre-confirm the performance of the individual components of a device [1, 2].

To reduce the dimensions of a device is most important for high integration of individual devices. In the case of electronic circuits, it is possible to reduce the dimensions of a device up to a few tens of nanometers. However, in the case of optical devices, it is difficult to do so because of the diffraction limit of light [3]. One way of overcoming the diffraction limit is the use of surface plasmon optics. Surface plasmon phenomena occur at the interface of dielectric and metal. Since surface plasmon polaritons are not affected by the diffraction limit, it is possible to guide and control light at a nanoscale [4]. In particular, surface plasmon phenomena become remarkable when a device is made of nano-sized metal, and optical devices based on nano-sized metal may have higher efficiency of

integration than conventional devices. Thus, it is anticipated that optical devices based on nano-sized metal may have an important position in the field of optics.

In this thesis, in accordance with the trend of research on nano-photonics, dielectric-loaded surface plasmon polariton waveguides, which are a representative nano-plasmonic waveguide, are studied. First, in order to reduce the high loss of coupling between a photonic waveguide and a plasmonic waveguide, I select the SU8 for the material of the waveguide core. The coupling loss is further reduced by modifying the waveguide into a double-dielectric-loaded surface plasmon polariton (D^2LSPP) waveguide. The D^2LSPP waveguide can be coupled to the photonic waveguide with higher efficiency. Moreover, the coupling region length is much reduced. Second, 60º fan-shaped bends of DLSPP waveguides are proposed. By reducing a bending angle from 90° to 60° and introducing a fan-shaped structure. Finally, a fabrication process of DLSPP waveguide based on the commercially available photoresist SU8 is developed.

1.1 Optical characteristics of metal

The theoretical understanding of the origin of optical properties of surface plasmon begins with Drude model of metal [5, 6]. A plasma is a medium with equal concentration of positive and negative charges, of which at least one charge is mobile. A plasma oscillation is when one group of charges moves relative to the other, such as in a metal with electrons moving with respect to the positive ions. The quantum of the plasma oscillation is a quasi-particle referred to as a plasmon. The frequency response of metal can be described by Drude model, considering the metal to be formed of a mass of positively charged ions from which a number of free electrons were detached. The conduction electrons do not interfere with each other and the only possible interaction is the instantaneous collision between a free electron and an ion, which happen with a fixed probability per unit time. The relative permittivity of the metal is as follow.

$$\varepsilon_m = 1 - \frac{\omega_p^2}{\omega\left(\omega + \frac{i}{\tau}\right)} = 1 - \frac{\omega_p^2}{\omega^2 + \tau^{-2}} + i\frac{\omega_p^2 \tau}{\omega(\omega + \omega^2\tau^2)}, \omega^p = \sqrt{\frac{Ne^2}{m\varepsilon_0}} \tag{2.1}$$

where, ω_p is the plasma frequency having different value in different metals. τ is the average time between collisions for the electron, m is the mass of the electron and e is the elementary charge. N is the number of free electrons per unit volume. This is commonly called the Drude model for the dielectric constant of the metal since it is based on the Drude theory of electrical conductivity. If the collision time becomes infinite, then the relative permittivity of the metal simplifies to

$$\varepsilon_m = 1 - \frac{\omega_p^2}{\omega^2} \tag{2.2}$$

Eq. 2.2 represents the relative permittivity is positive for $\omega > \omega_p$ and negative for $\omega < \omega_p$. At optical frequency, the Dude model of the permittivity of the noble metal, such as silver, gold and copper, predicts a permittivity.

1.1.1 Maxwell's equations of macroscopic electromagnetism

The interaction of the metal and the electromagnetic field can be understood as the Maxwell's equations. Accordingly, we first need to know the basic equations governing the electromagnetic response, the macroscopic Maxwell equations. The advantage of this phenomenological approach is that details of the fundamental interactions between charged particle inside media and electromagnetic fields need not be taken into account since the rapidly varying microscopic fields are averaged over distances much larger than the underlying microstructure.

So, we take as a starting point the macroscopic Maxwell's equations in the following form:

$$\nabla \cdot \mathbf{D} = \rho_{ext} \tag{2.3}$$

$$\nabla \cdot \mathbf{B} = 0 \tag{2.4}$$

$$\nabla \times \mathbf{E} = -\frac{\partial \mathbf{B}}{\partial t} \tag{2.5}$$

$$\nabla \times \mathbf{H} = \mathbf{J}_{\text{ext}} + \frac{\partial \mathbf{D}}{\partial t} \tag{2.6}$$

where, the D represents the dielectric displacement, E represents the electric field, H represents the magnetic field, B represents the magnetic induction or magnetic flux density with the external charge and current densities ρ_{ext} and J_{ext}.

The four macroscopic fields are expressed via the polarization **P** and magnetization **M** by

$$\mathbf{D} = \varepsilon_0 \mathbf{E} + \mathbf{P} \tag{2.7}$$

$$\mathbf{H} = \frac{1}{\mu_0}\mathbf{B} - \mathbf{M} \tag{2.8}$$

where, ε_0 is the electric permittivity and μ_0 is the magnetic permeability of vacuum. In this text we only treat nonmagnetic media, so we need not consider magnetization **M**. P represents the electric dipole moment per unit volume. It is related to the internal charge density via $\nabla \cdot \mathbf{P} = -\rho$. Charge conservation requires that it is bound through the current density and internal charge:

$$\mathbf{J} = \frac{\partial \mathbf{P}}{\partial t} \tag{2.9}$$

This approach has the great advantage of the macroscopic electric field which will contain all polarization effects.

$$\nabla \cdot \mathbf{E} = \frac{\rho_{\text{tot}}}{\varepsilon_0} \tag{2.10}$$

In the following, we will limit ourselves to linear, isotropic and nonmagnetic media. We can define the constitutive relations

$$\mathbf{D} = \varepsilon_0 \varepsilon \mathbf{E} \tag{2.11}$$

$$\mathbf{B} = \mu_0 \mu \mathbf{H} \tag{2.12}$$

ε represents the dielectric constant or relative permittivity and μ = 1 represents the relative permeability of the nonmagnetic medium. The D and E can be defined using the dielectric susceptibility χ.

$$\mathbf{P} = \varepsilon_0 \chi \mathbf{E} \tag{2.13}$$

Finally, we need to mention an important constitutive between internal current density **J** and the electric filed **E**, defined via the conductivity σ by

$$\mathbf{J} = \sigma \mathbf{E} \tag{2.14}$$

1.2 Surface Plasmon Polaritons (SPPs) at metal-dielectric interface

Surface plasmon polaritons (SPPs) are electromagnetic waves which travel along metal-dielectric interfaces [7]. Such electromagnetic wave vibration in the conductor of the electron plasma generated through electromagnetic coupling. I describe the fundamental of surface plasmon polaritons at single interfaces in metal-dielectric structure.

Fig. 1-1 shows the simplest structure sustaining SPPs. This structure has a dielectric constant ε_2 of a positive real value with non-absorbing half space (z > 0). And the adjacent half space (z < 0) has a dielectric constant ε_1 consists of a metal. We want to see in order to propagating wave to interface with the evanescent decay in the perpendicular z-direction. We first look at transverse-magnetic (TM) solutions.

$$H_y(\mathrm{z}) = A_2 e^{i\beta x} e^{-k_2 z} \tag{2.15a}$$

$$E_x(\mathrm{z}) = iA_2 \frac{1}{\omega \varepsilon_0 \varepsilon_2} k_2 e^{i\beta x} e^{-k_2 z} \tag{2.15b}$$

$$E_z(\mathrm{z}) = -A_2 \frac{\beta}{\omega \varepsilon_0 \varepsilon_2} e^{i\beta x} e^{-k_2 z} \tag{2.15c}$$

for z > 0 and

$$H_y(\mathrm{z}) = A_1 e^{i\beta x} e^{k_1 z} \tag{2.16a}$$

$$E_x(\mathrm{z}) = -iA_1 \frac{1}{\omega \varepsilon_0 \varepsilon_1} k_1 e^{i\beta x} e^{k_1 z} \tag{2.16b}$$

$$E_z(\mathrm{z}) = -A_1 \frac{\beta}{\omega \varepsilon_0 \varepsilon_1} e^{i\beta x} e^{k_1 z} \tag{2.16c}$$

for z < 0.

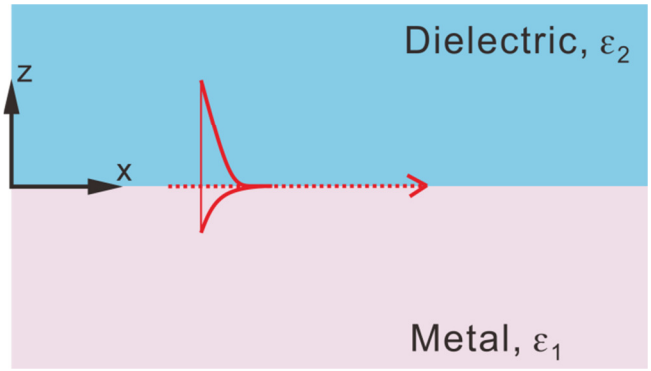

Fig. 1-1. Structure for SPP propagation interface between a metal and a dielectric.

Second, we look at transverse-electric (TE) solutions. The field components are

$$E_y(\mathrm{z}) = A_2 e^{i\beta x} e^{-k_2 z} \tag{2.15a}$$

$$H_x(\mathrm{z}) = -iA_2 \frac{1}{\omega\mu_0} k_2 e^{i\beta x} e^{-k_2 z} \tag{2.15b}$$

$$H_z(\mathrm{z}) = A_2 \frac{\beta}{\omega\mu_0} e^{i\beta x} e^{-k_2 z} \tag{2.15c}$$

for z > 0 and

$$E_y(\mathrm{z}) = A_1 e^{i\beta x} e^{k_1 z} \tag{2.16a}$$

$$H_x(\mathrm{z}) = iA_1 \frac{1}{\omega\mu_0} k_1 e^{i\beta x} e^{k_1 z} \tag{2.16b}$$

$$H_z(\mathrm{z}) = A_1 \frac{\beta}{\omega\mu_0} e^{i\beta x} e^{k_1 z} \tag{2.16c}$$

for z < 0. Leads to the condition of continuity of H_x and E_y at the interface

$$\mathrm{A}_1(k_1 + k_2) = 0 \tag{2.14}$$

It requires Re $[k_1] > 0$ and Re $[k_2] > 0$, this condition is only satisfied if $A_1 = 0$, so that $A_1 = A_2 = 0$. Consequently, the surface plasmon polariton can be propagated by TM polarized wave. Thus, no exists TE polarization mode at the surface.

1.3 Plasmonic waveguides

Since an SPP is coupled to the collective oscillation of free electrons in a metal surface, its wavelength can be made much shorter than the free-space wavelength λ. Because of this nature of SPPs, SPP-based nanoplasmonic waveguides are believed to overcome the diffraction limit: they can support a mode which has a mode area much smaller than $(\lambda/2)^2$ [8]. Thus a variety of nanoplasmonic waveguides have been investigated. A few examples are metal-insulator-metal (MIM) waveguides [9-11], metal-insulator-silicon-insulator-metal (MISIM) waveguides [12-16], and dielectric-loaded SPP (DLSPP) waveguides [17-19].

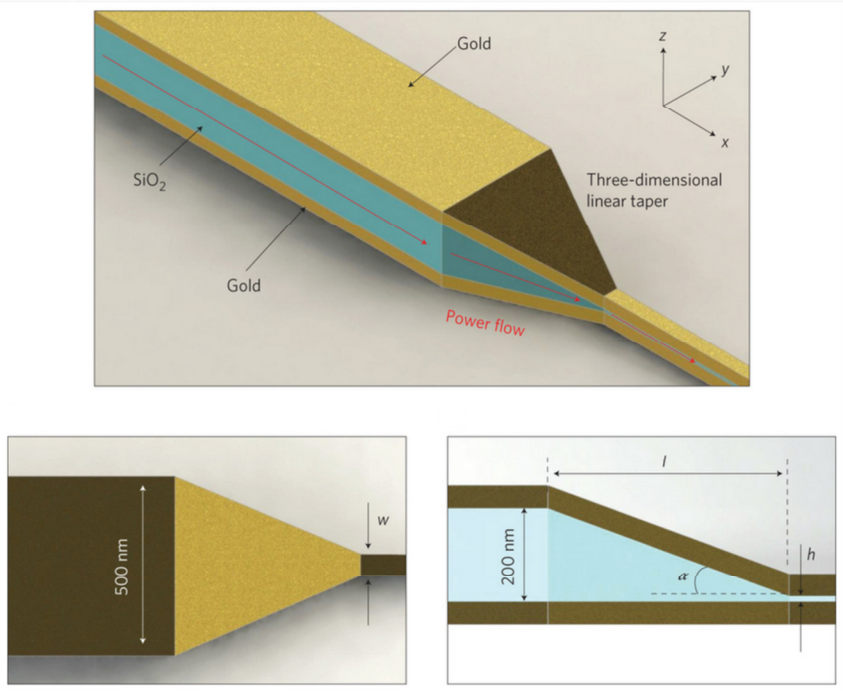

Fig. 1-2. Example structure of metal-insulator-metal (MIM) waveguide [11].

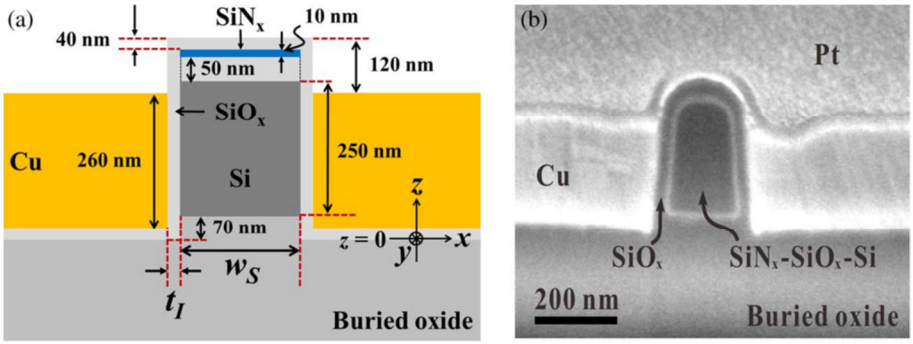

Fig. 1-3. Example structure metal-insulator-silicon-insulator-metal (MISIM) waveguide [15]. (a) Schematic diagram of the cross-sectional structure. (b) SEM image of the cross section of the fabricated MSIM waveguide.

Chapter 2

Coupling between a Photonic Waveguide and a Dielectric-Loaded Surface Plasmon Polariton (DLSPP) Waveguide

In this chapter, i theoretically investigate how to improve the efficiency of the coupling between a DLSPP waveguide and a photonic waveguide and reduce the length of the coupling region, l_t. And, i try to do so by employing a dielectric with a refractive index higher than those of the previous loaded dielectrics. Then, to further improve the coupling efficiency and reduce the coupling region length, i modify the DLSPP waveguide based on the high-index dielectric. The modified DLSPP waveguide is called a double-dielectric-loaded SPP (D^2LSPP) waveguide. I discuss the characteristics of the D2LSPP waveguide and the coupling between the D^2LSPP waveguide and the photonic waveguide with the high-index dielectric core.

2.1 DLSPP waveguide

Compared to MIM or MISIM waveguides, a DLSPP waveguide has a rather large mode area similar to $[\lambda/(2n_d)]^2$, where n_d is the refractive index of a loaded dielectric. However, it can be much more easily implemented than MIM or MISIM waveguides. In addition, it has a smaller propagation loss than MIM or MISIM waveguides. Moreover, it is a good platform for realizing functional nanoplasmonic devices with various dielectrics (e.g. electrooptic or nonlinear polymer) loaded. Because of these features, DLSPP-waveguide-based directional couplers [20], ring resonators [21, 22], Mach-Zehnder interferometers [22, 23] have been developed.

Although the propagation loss of a DLSPP waveguide is relatively small, it is still much larger than that of a photonic waveguide. This situation requires a hybrid structure in which transmission of a light signal is assigned to photonic waveguides and control of the light signal is done by a DLSPP waveguide device in a compact region [24]. Therefore, it is essential to efficiently couple a DLSPP waveguide to a photonic waveguide. If the same material is used for the loaded dielectric of a DLSPP waveguide and the core of a photonic waveguide, the size mismatch between the loaded dielectric in a rectangular shape and the core should be solved. The smaller n_d is, the larger the dimensions of the core are, and the more serious the mismatch problem becomes. When poly(methyl methacrylate) (PMMA) of refractive index 1.49 was used, this problem was solved by making the 1-μm-high core and loaded dielectric on a substrate with a low refractive index and increasing the width of the loaded

dielectric, w_d, to the width of the core, w_p, over a distance l_t [25]. When the nanoimprint lithography resist mr-NIL 6000 of refractive index 1.523 was used, both w_d and the height of the loaded dielectric, h_d, are increased to w_p and the height of the core, h_p, respectively [26]. However, in both the cases, l_t is large (> 20 μm), and the coupling loss between a DLSPP waveguide and a photonic waveguide is large (> 2 dB). The following two structures are shown in Fig. 2-1.

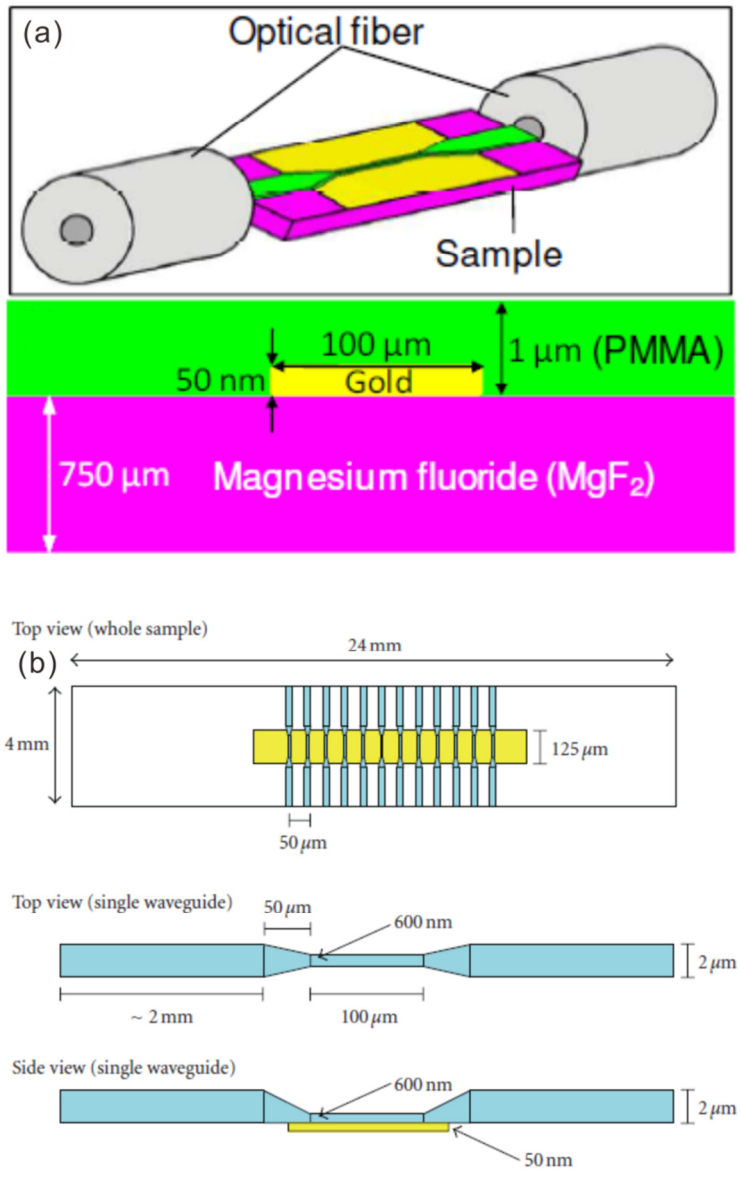

Fig. 2-1. The existing DLSPP waveguide structure [25, 26].

2.1.1 Waveguide structure

The investigated photonic waveguide and DLSPP waveguide are schematically shown in Fig. 2-2 (a) and (b), respectively. The two waveguides are on the same substrate. Its refractive index n_s was set to that of commercially available polymer Exguide™ LFR (ChemOptics Inc.) such that n_s = 1.375. The loaded dielectric of the DLSPP waveguide is on the gold film with a thickness t_d, which was set to 0.1 μm. The refractive index of gold is 0.559 + *i*9.81 at λ = 1.55 μm. It is assumed that $h_p = h_d + t_d$. In the following discussion, λ = 1.55 μm.

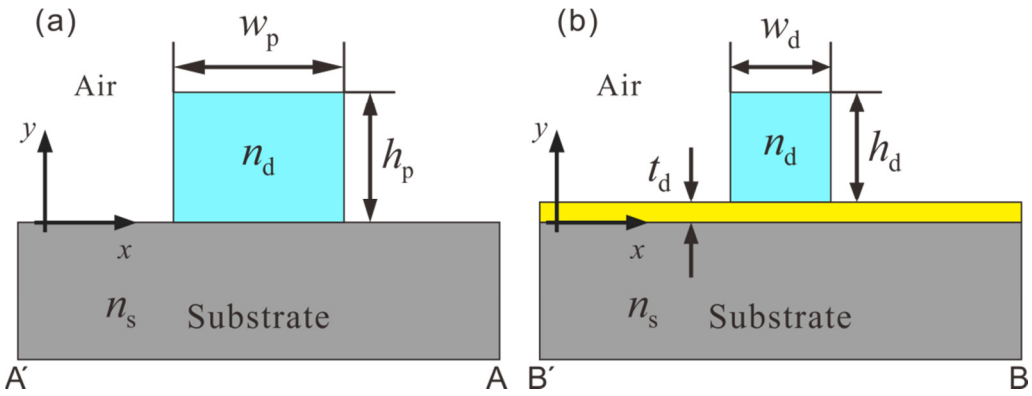

Fig. 2-2. (a) Cross-sectional structure of the photonic waveguide. (b) Cross-sectional structure of the DLSPP waveguide. It is assumed that $h_p = h_d + t_d$.

2.1.2 Design of the photonic waveguide

Using the mode solver FIMMWAVE (Photon Design) based on the finite element method, we found the region of (h_p, w_p) which allows the photonic waveguide to support only the fundamental transverse-magnetic (TM) mode TM_{p00}. The two regions for n_d = 1.49 and 1.57 are shown in Fig. 2-3 (a). TM_{p00} is cut off for (h_p, w_p) on the lower curve of each region. The first higher-order mode, TM_{p10} is cut off for (h_p, w_p) on the upper curve of each region. (h_p, w_p) close to the upper curve of each region should be chosen to ensure that TM_{p00} is well guided. However, we cannot choose an arbitrarily large value of h_p due to two constraints. The one constraint is related to fabrication of the loaded dielectric pattern. We checked that the fundamental TM mode of the DLSPP waveguide, TM_{d00} is most tightly confined in the x direction if $w_d \cong 0.5$ μm, which is approximately equal to $\lambda/(2n_d)$. The larger the ratio of h_d to w_d is, the harder the fabrication is. If the achievable ratio is 2, then h_d should be smaller than 1 μm. The second constraint is related to the single-mode operation of the DLSPP waveguide. Fig. 2-2 (b) and (c) show the intensity distributions of TM_{d00} and the higher-order mode TM_{d01} for h_d = 1 μm, w_d = 0.5 μm, and n_d = 1.57. h_d should be smaller than the specific value for which TM_{d01} is cut off. It is 0.85 and 1.05 μm for n_d = 1.57 and 1.49, respectively. The values of h_p, determined from these specific values, are denoted by the vertical dotted lines in Fig. 2-2 (a).

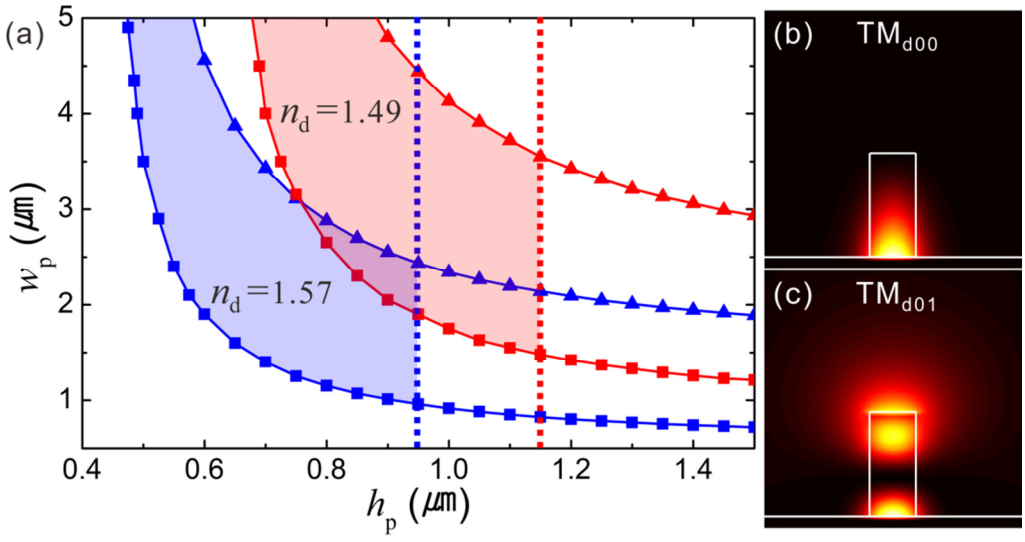

Fig. 2-3. (a) Region of width w_p and height h_p for which the photonic waveguide supports only the fundamental TM mode TM_{p00}. TM_{p00} is cut off if w_p and h_p are on the lower curve with square symbols. The first higher-order mode TM_{p10} is cut off if w_p and h_p are on the upper curve with triangle symbols. If h_p is on the right of the dotted line, the DLSPP waveguide supports the first higher-order mode TM_{d01}. (b) and (c) Intensity profiles of TM_{d00} and TM_{d01} of the DLSPP waveguide for h_d = 1 μm, w_d = 0.5 μm and n_d = 1.57.

If n_d = 1.49, w_p needs to be large (e.g. > 5 μm) for a moderate value of h_p (e.g. 0.9 μm). Then, l_t needs to be large, and the coupling efficiency becomes low. w_p can be small if h_p is chosen to be close to 1.15 μm. However, in this case, the first constraint seems not to be satisfied. In the case of n_d = 1.57, the photonic waveguide with w_p = 2.5 μm and h_p = 0.9 μm supports only TM_{p00}, and TM_{p00} is far from cut-off. The result in Fig. 2 shows that n_d needs to be large to reduce w_p and h_p such that the size mismatch problem can be alleviated to some extent. However, if n_d is too large, it becomes inefficient to launch light into the photonic waveguide. In addition, there are few waveguide materials which have a large refractive index and can be easily processed. The negative photoresist SU8 has a refractive index of 1.57; it can be patterned by using either optical lithography or e-beam lithography [27, 28]; it has been used for optical waveguides [29]. Therefore, n_d was set to 1.57, and w_p, h_p, w_d, and h_d were determined to be 2.5, 0.9, 0.5, and 0.8 μm, respectively. The propagation loss α_d of the DLSPP waveguide is 0.13 dB/μm.

2.2 Coupling between a DLSPP waveguide and a photonic waveguide

2.2.1 Coupling loss between a DLSPP waveguide and a photonic waveguide

Using the finite-difference time domain (FDTD) method (FDTD solutions, Lumerical Inc.), the coupling structure was analyzed. The top view of the coupling structure photonic waveguide between DLSPP waveguide is shown in Fig. 2-4. TM_{p00} was launched at position P_1 in the photonic waveguide. For this input, the power transmittance in dB was calculated at position P_3 in the DLSPP waveguide; P_3 is at a distance l_d from position P_2 where the coupling structure ends. The coupling loss of the coupling structure is defined as the subtraction of the straight DLSPP waveguide loss given by $\alpha_d \times l_d$ from the negative of the transmittance. The calculated coupling loss is shown as a function of l_t in Fig. 2-5. The minimum coupling loss is 2.3 dB if l_t = 3 μm. This value of l_t is about one tenth of the previous values in [25, 26], and the coupling loss is smaller than that in [25].

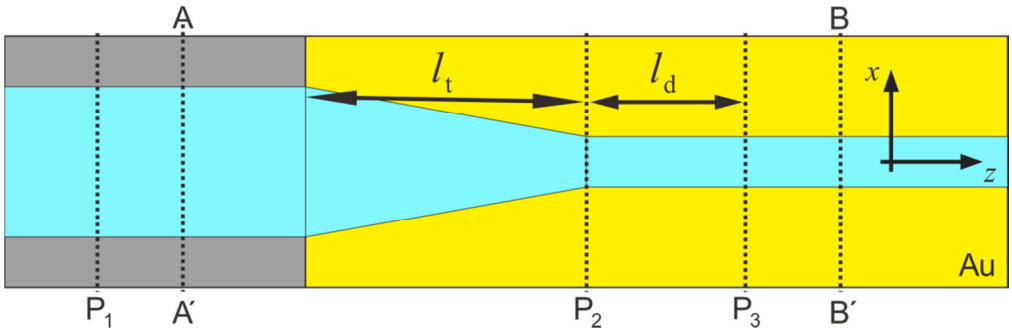

Fig. 2-4. Top view of the coupling structure between the photonic waveguide and the DLSPP waveguide.

There is one thing that we need to consider regarding the optimal value of l_t. The relations of the transmittance to l_d for l_t = 3 and 8 μm are shown in Fig. 2-6 (a). If l_t = 8 μm, the relation does not deviate much from the straight line which has a slope equal to $-\alpha_d$. However, the relation for l_t = 3 μm clearly deviates from the straight line when l_d is smaller than 10 μm. If l_t = 3 μm, considerable radiation modes are still excited at P_2 although TM_{d00} is most efficiently excited. In contrast, excitation of radiation modes other than TM_{d00} at P_2 is suppressed if l_t = 8 μm. This is confirmed by the distributions of the magnitude of the magnetic field at P_2 for l_t = 3 and 8 μm, which are shown in Fig. 2-6 (b) and (c), respectively. We checked that the relation of the transmittance to l_d for l_t = 7 μm deviates more from the straight line than that for l_t = 8 μm. Therefore, l_t should be 3 μm for the maximum excited power of TM_{d00}, but l_t should be 8 μm for the suppression of excitation of radiation modes other than TM_{d00}. The coupling loss for l_t = 8 μm is 2.8 dB, which is still smaller than that in [25].

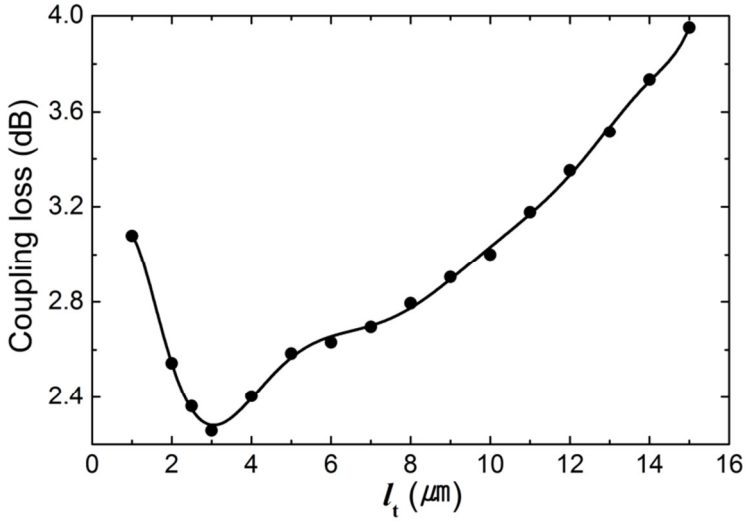

Fig. 2-5. Relation of the coupling loss to the coupling region length l_t. The circle symbols are obtained from the calculation based on the FDTD method. The solid line is a guide for the eyes.

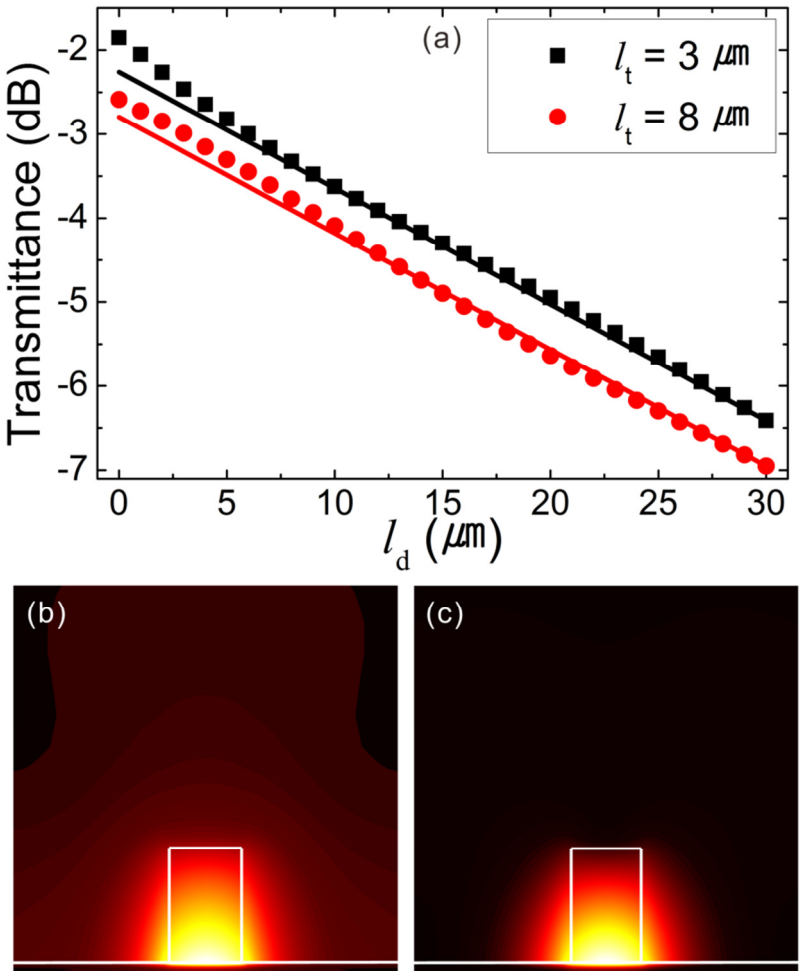

Fig. 2-6. (a) Transmittance at P_3 vs. l_d. The symbols are obtained from the calculation based on the FDTD method. The solid straight lines have a slope equal to $-\alpha_d$, and they pass the calculated transmittance at l_d = 30 μm. (b) and (c) Distributions of the magnitude of the magnetic field at P_2 for l_t = 3 and 8 μm.

2.3 Proposed double dielectric-loaded surface plasmon polariton (D^2LSPP) waveguide

2.3.1 Waveguide structure and characteristic

The coupling loss is mainly caused by the fact that TM_{d00} does not have fields below $y = 0$ μm but TM_{p00} does so. Therefore, the fields of TM_{p00} below $y = 0$ should be reduced to decrease the coupling loss further. This can be achieved by increasing h_p. However, the increase of h_p results in that of h_d such that TM_{d01} is supported by the DLSPP waveguide. To solve this problem, we modify it into the D^2LSPP waveguide shown in Fig. 2-7 (a). The second dielectric of refractive index n_d' and height h_d' is placed in between the gold film and the loaded dielectric. $n_d' < n_d$, and $h_p = h_d + h_d' + t_d$. The intensity distribution of the fundamental TM mode, which is also denoted by TM_{d00}, of the D^2LSPP waveguide is shown in Fig. 2-7 (b) for $n_d' = 1.45$ and $h_d' = 0.4$ μm. It is similar to that of the DLSPP waveguide. Because of the second dielectric, we can increase h_p to some extent while maintaining the single-mode operation of the D^2LSPP waveguide. In addition, the fields of TM_{d00} shift upwards (see Fig. 2-8 (c)). Consequently, TM_{p00} matches better TM_{d00} of the D^2LSPP waveguide than TM_{d00} of the DLSPP waveguide.

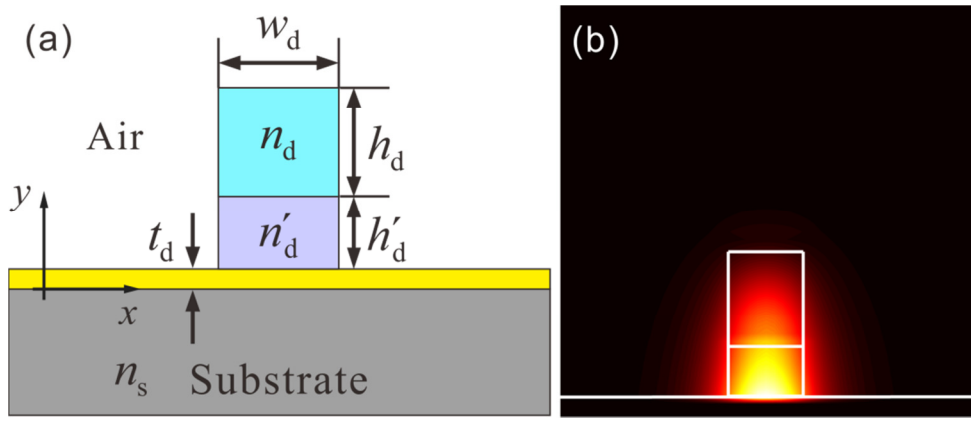

Fig. 2-7. (a) Cross-sectional structure of the D^2LSPP waveguide. (b) Intensity profile of the fundamental TM mode TM_{d00} of the D^2LSPP waveguide for $h_d = 0.6$ μm, $h_d' = 0.4$ μm, and $n_d' = 1.45$.

The second dielectric is determined to be the negative e-beam resist hydrogen silsesquioxane (HSQ) such that $n_d' = 1.45$. HSQ has also been used for optical waveguides [30]. We expect that it would be possible to pattern simultaneously SU8 and HSQ by using e-beam lithography. We checked that the D^2LSPP waveguide supports only TM_{d00} when $h_d + h_d' \leq 1$ μm and $h_d' \geq 0.2$ μm. With h_d and h_d'

varied under the constraint that $h_d + h_d' = 1$ μm and $h_d' \geq 0.2$ μm, the effective mode area and propagation loss of TM_{d00} were calculated. The effective mode area is defined as $\left[\int W(\mathbf{r})dA\right]^2 / \left[\int W(\mathbf{r})^2 dA\right]$, where $W(\mathbf{r})$ is the energy density [31]. The calculated effective mode area and propagation loss are shown with respect to h_d' in Fig. 2-8 (a). As h_d' increases, the fields of TM_{d00} become weak on the gold surface, and they are more widely distributed in both the dielectrics. This can be confirmed from the distributions of the magnitude of the *y*-component of the electric field of TM_{d00}, $|E_y|$, along the vertical centerline of the loaded dielectric; they are shown in Fig. 2-8 (b) and 4(c) for h_d' = 0.2 and 0.4 μm, respectively. Hence, the effective mode area increases, and the propagation loss decreases. However, if h_d' increases further, the fields become strong on the gold surface again as shown in the distribution of $|E_y|$ for h_d' = 0.8 μm in Fig. 4(d). In other words, the D^2LSPP waveguide behaves like the DLSPP waveguide. Therefore, the effective mode area decreases, and the propagation loss increases.

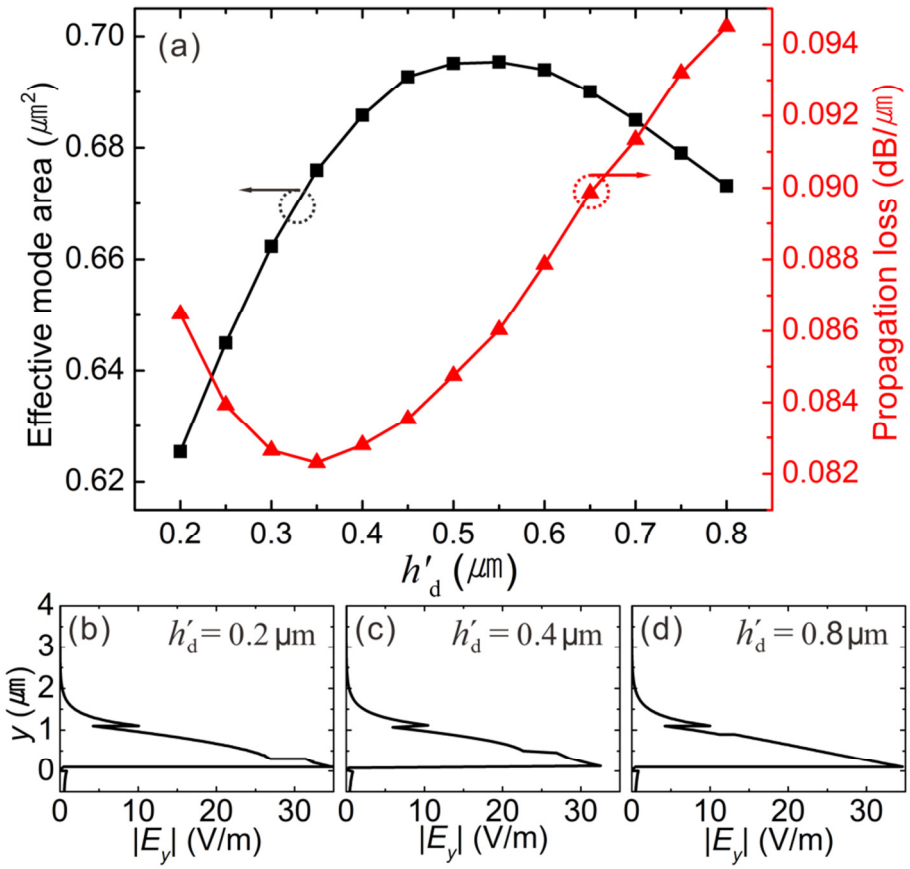

Fig. 2-8. (a) Relations of the effective mode area and propagation loss of TM_{d00} to h_d'. (b), (c), and (d) show the distributions of the magnitude of the *y*-component of the electric field of TM_{d00}, $|E_y|$, along the vertical centerline of the loaded dielectric for h_d' = 0.2, 0.4 and 0.8 μm, respectively.

2.4 Coupling between a D^2LSPP waveguide and a photonic waveguide

2.4.1 Coupling loss between a D^2LSPP waveguide and a photonic waveguide

The D^2LSPP waveguide is connected to the photonic waveguide in the same way as the DLSPP waveguide: the top view of the coupling structure for the D^2LSPP waveguide is the same as shown in Fig. 2-4. The coupling loss was calculated as a function of h_d' while l_t was set to 4 μm. The calculation result is shown in Fig. 2-9. When h_d = 0.6 μm and h_d' = 0.4 μm, the coupling loss is minimum equal to 1.1 dB. Actually, we checked that if l_t = 4 μm, the coupling loss is minimized for all the combinations of h_d and h_d'. Consequently, the use of the D^2LSPP waveguide with h_d = 0.6 μm and h_d' = 0.4 μm enables the coupling loss to be reduced from 2.3 dB to 1.1 dB and the propagation loss α_d to be reduced from 0.13 dB/μm to 0.083 dB/μm. However, l_t increases from 3 μm to 4 μm, and the effective mode area increases from 0.5 μm^2 to 0.68 μm^2. Interestingly, in the case of the D^2LSPP waveguide, TM_{d00} is excited not only most efficiently but also almost without excitation of radiation modes if l_t = 4 μm. This can be checked from Fig. 2-10, which shows the transmittance at P_3 in the D^2LSPP waveguide with h_d = 0.6 μm and h_d' = 0.4 μm as a function of l_d for l_t = 4 μm. The transmittance decreases almost linearly, following the straight line with a slope equal to $-\alpha_d$. The intensity profile at P_2 shown in the inset indicates that TM_{d00} is dominantly excited at the position. Therefore, the D^2LSPP waveguide is better for efficient excitation of TM_{d00} without radiation modes through the shorter coupling region than the DLSPP waveguide.

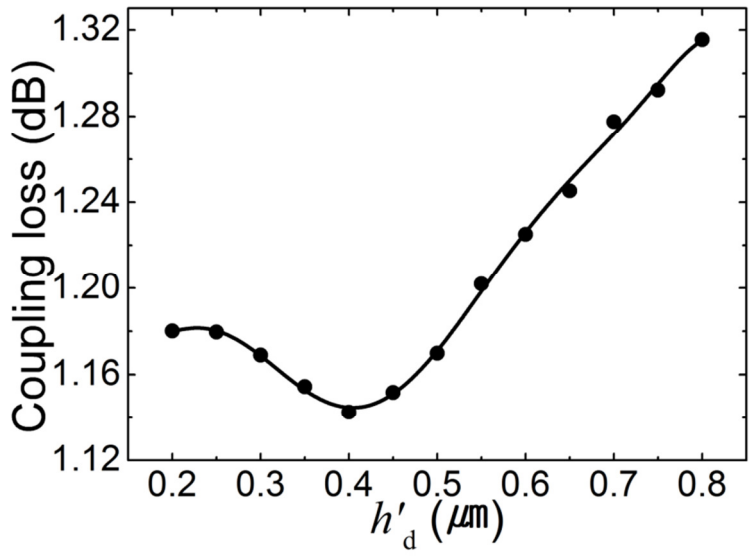

Fig. 2-9. Relation of the coupling loss to h'_d. The circle symbols are obtained from the calculation based on the FDTD method. The red solid line is a guide for the eyes.

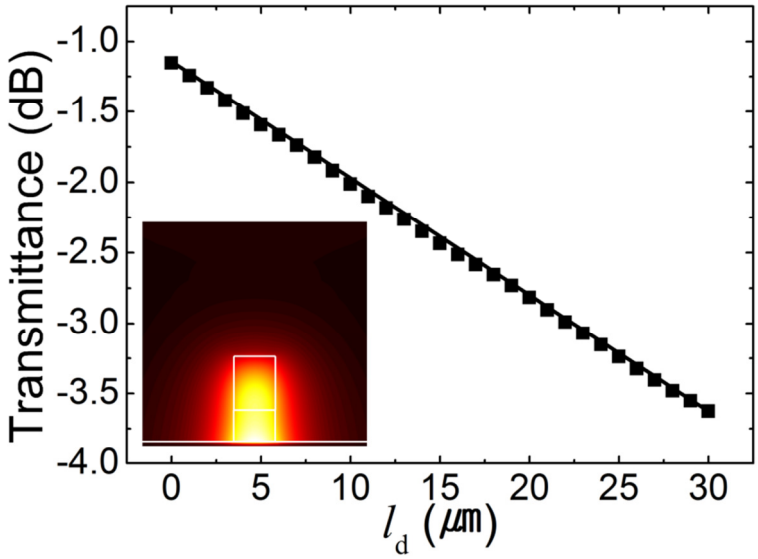

Fig. 2-10. Transmittance at P_3 vs. l_d. The circle symbols are obtained from the calculation based on the FDTD method. The solid straight line has a slope equal to $-\alpha_d$, and they pass the calculated transmittance at $l_d = 30$ μm. The inset shows the distributions of the magnitude of the magnetic field at P_2.

Chapter 3

60º fan-shaped bends of dielectric-loaded surface plasmon polariton waveguide

Bend structure of DLSPP waveguide is an essential element for the implementation of the various functional DLSPP waveguide and optical connection. Thus, much research for the bend structure was conducted [32]. However, almost all the previous researches are conducted by based on the 90° curved bend but it has a disadvantage that has a large bend radius of about 5 ~ 6 μm. Result of previous research is shown in Fig. 3-1. Therefore, in this chapter, I proposed 60° fan-shaped bends based on the DLSPP waveguide structure, and I investigated for their characteristic.

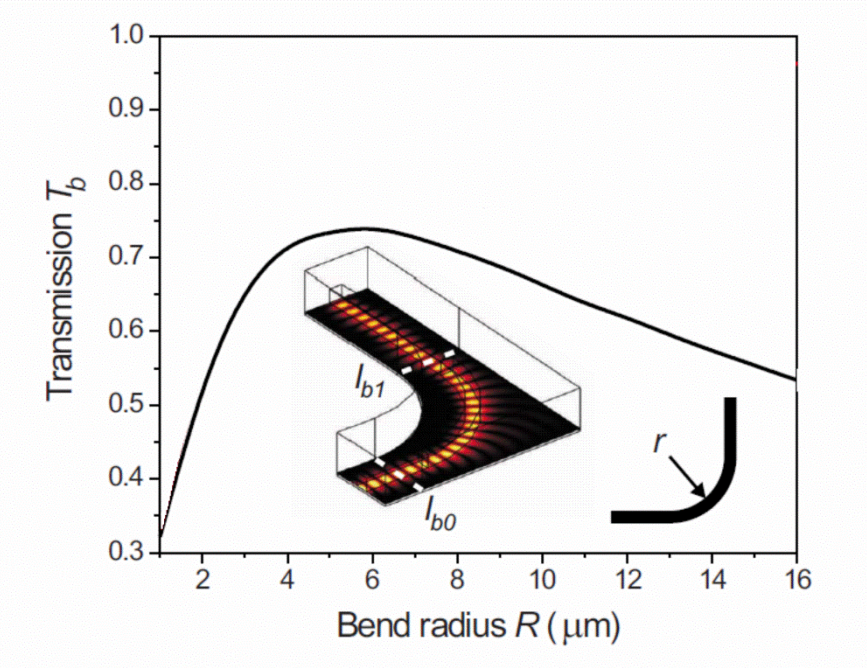

Fig. 3-1. Relations of the transmission to the bend radius R of the 90º curved bend [32].

3.1 Bend structure

The basic structure of the waveguide is the same as the proposed in chapter 2, the cross section structure shown in Fig. 3-2 (a). 60 ° curved bend and 60 ° fan-shaped bend of the proposed structure on the xz plane is shown in Fig. 3-2 (b) and (c), respectively. The parameters for the structure used in the simulation are as follows: w_d = 0.5 μm, h_d = 0.8 μm, t = 0.1 μm, n_c = 1.57, n_s = 1.375. The refractive index of gold is 0.559 + i9.81 at λ = 1.55 μm.

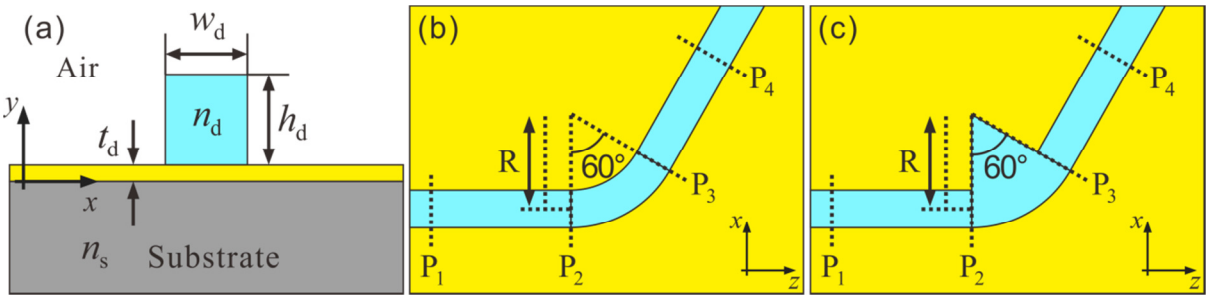

Fig. 3-2. (a) Cross-sectional structure of the DLSPP waveguide. (b) 60º curved bend of the DLSPP waveguide. (c) Proposed 60º fan-shaped bend of the DLSPP waveguide.

3.2 Bend characteristics

Using the finite-difference time domain (FDTD) method (FDTD solutions, Lumerical Inc.), the 60 ° curved bend and 60 ° fan-shaped bend structure was analyzed. The DLSPP mode launched from P_1 to a suitable distance away from the point P_2 that bend is started. For this input, the transmission was calculated at position P_4 the appropriate distance away from the point P_3 that bend ends. By subtracting propagation loss between P_1 and P_2 and between P_3 and P_4 from this transmission, we can calculate transmission only for the bend between P_2 and P_3. The relations of transmission to bend radius for 60° curved bend and 60° fan-shaped curved bend are shown in Fig 3-3. In the case of 60° curved bend, the transmission is maximum value at the 4.5 μm bend radius. In case of the 60° fan-shaped bend, the transmission is maximum value at the 2.25 μm bend radius, with the excess loss of 0.76 dB. Fig 3-4 (a) and (b) show the E_z field distribution for the bend radius R at 0.75 μm, 2.5 μm based on the 60° fan-shaped bend. It is possible to see that much fields are escaping after the bend structure for the 0.75 μm radius. It can be confirmed that the mode is propagated along the bend structure at 2.5 μm bend radius. Fig. 3-1 shows the transmission result in accordance with a bending radius of 90° curved bend. It was confirmed that 60° fan-shaped bend can be reduced the excess

losses and the bend radius compared to previous research.

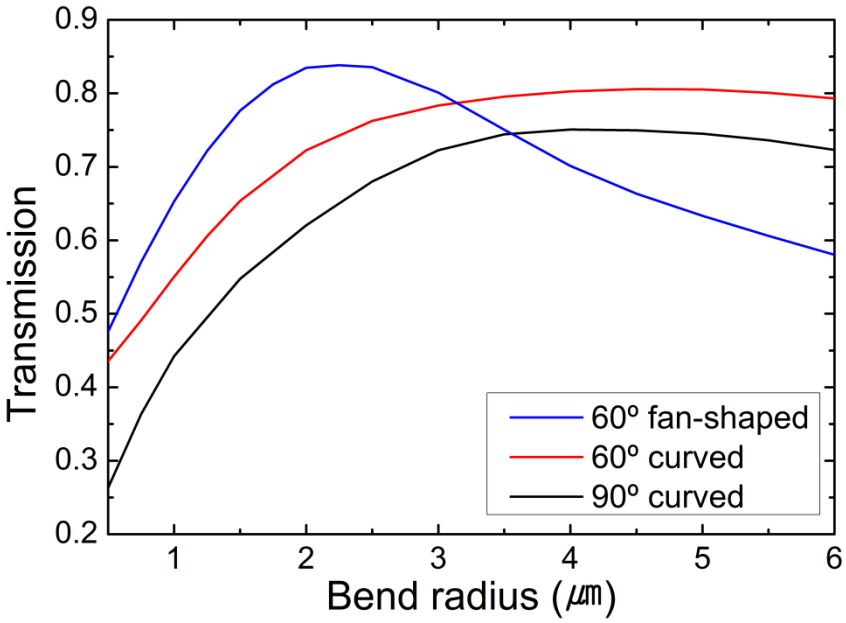

Fig. 3-3. Relations of the transmission to the bend radius R of the 90º curved bend, 60º curved bend and 60º fan-shaped curved bend.

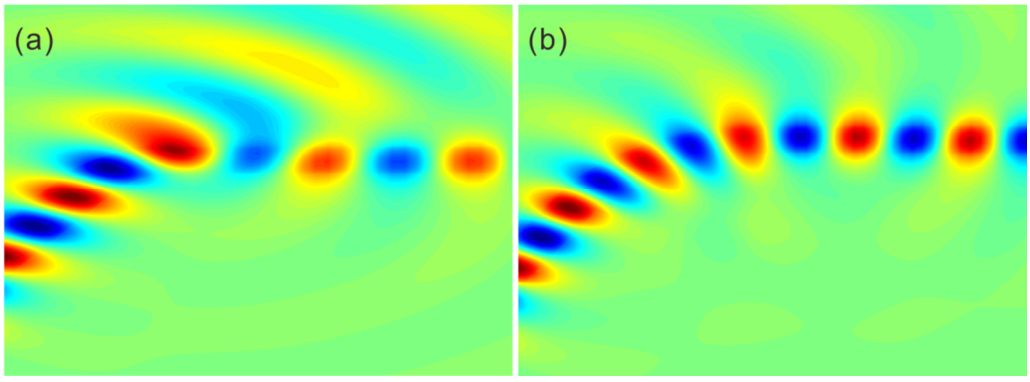

Fig. 3-4. Distributions of the magnitude of the z-component of the electric field of 60º fan-shaped curved bend of the DLSPP waveguide. (a) R = 0.75 μm. (b) R = 2.5 μm.

Chapter 4

Realization of DLSPP waveguides

4.1 Fabrication process of DLSPP waveguides

The proposed structure of the waveguide was fabricated by the process in Fig 4-1 and Fig 4-2. The substrate material of DLSPP waveguide structure is a polymer manufactured by Chemoptics Exguide™ LFR was used. Exguide™ LFR is photoactive UV curable resins based on perfluorinated acrylate. This is applicable to optical waveguide devices and optical thin film applications. These coating resins have low optical loss for optical communication wavelengths, small birefringence and excellent environment stability. To be used for various waveguide structures, precise and continuous control of the refractive index can be available achieved by blending technique with standard polymer solutions.

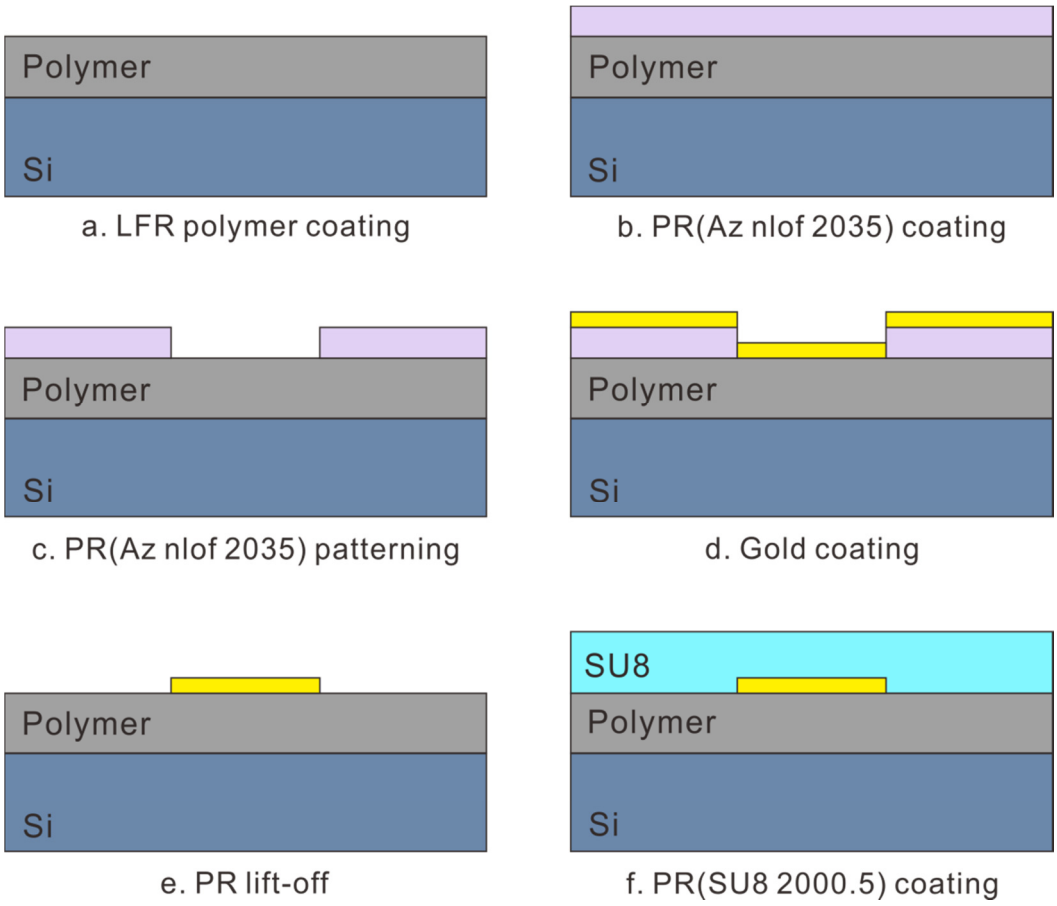

Fig. 4-1. Fabrication process of DLSPP waveguide (1).

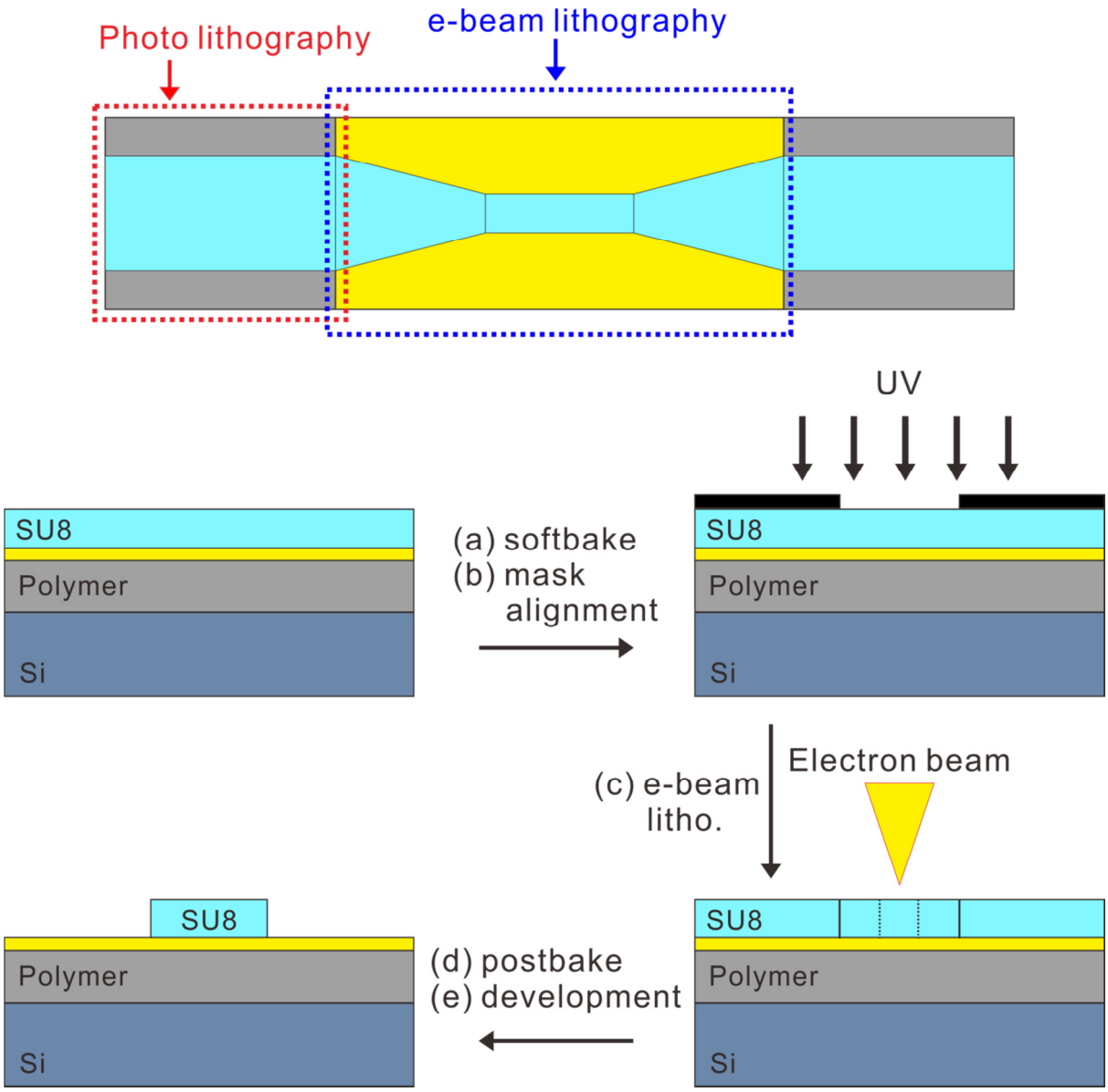

Fig. 4-2. Fabrication process of DLSPP waveguide (2).

Refractive index of the polymer is 1.375 at a wavelength of 1.55 μm. In this experiment, the device can be easily produced by using a silicon wafer for spin coating with LFR polymer. Spin coated LFR polymer was cured using a UV exposure in a nitrogen environment. The LFR polymer that was used as a substrate material of the DLSPP waveguide was coated enough to thickness 12 μm to prevent the propagation loss of the surface plasmon mode of silicon wafer having a value of high refractive index of 3.4. If the polymer was not deposited enough to thickness at between the silicon wafer and waveguide, the coupling loss of the DLSPP waveguide that appears in the output stage are measured precariously. For the fabrication of gold layer photo resist (PR) lift-off method was used. Lift-off method was used by the negative PR as AZ nLOF 2035. When the expose using the embossed mask, the unexposed portion of PR is removed after the process. The most important step in the Lift-off is to

optimize the precise process condition for correct line width of gold to come out during the wet etching. First, PR of 3 μm thickness was spin-coated and the PR was cured at 105 ℃ for 90 second on a hotplate. Next, PR is patterned using a mask aligner, and the chrome mask that the pattern is formed. At this time, PR has a negative characteristic, that is removed the unexposed portions to UV light. After the patterning, the PR was cured again at 115 ℃ for 60 second on a hotplate. Next, PR is removed using a AZ-300MIF developer solution. After that, the gold layer of 100 nm thickness is deposited using the e-beam evaporator. The adhesion layer of the chrome was deposited together for to increase the adhesion between a polymer substrate and a gold layer. The deposition rate of the e-beam evaporator is 0.1 nm/s.

Patterning process is progressed by one step lithography. For the fabrication of the waveguide structure, SU8 2000.5 for 0.8 μm thickness was spin-coated and the SU8 was cured at 95 ℃ for 4 minutes on a hotplate. After that, photonic waveguide section is patterned using a mask aligner. And then DLSPP waveguide section is patterned directly by the e-beam lithography. And again SU8 was cured at the 95 ℃ for 2 minutes on a hotplate. Lastly the PR was developed.

4.2 Process Conditions

There are conditions to be careful in the fabrication process of in this study. First, adhesion problem between a metal and a substrate. To solve the adhesion problem, I added 0_2 plasma etching process using the reactive ion etching (RIE), before metal deposition process. Metal can be attached stably on the substrate after the lift off, through the etching process. Second, SU8 is influenced roughness of the pattern by depending on the baking temperature and time. Some of the attempted photolithography conditions shown in Table I. And Fig 4-3 shows SEM images of the waveguide patterns.

Table I. Process conditions for SU8 photolithography.

Sample	Soft bake	UV exposure [mJ/cm^2]	Post bake
#1	110 ℃, 1 min.	65	110 ℃, 1 min.
#2	110 ℃, 2 min.	65	110 ℃, 2 min.
#3	95 ℃, 4 min.	50	110 ℃, 1 min.
#4	95 ℃, 4 min.	45	110 ℃, 2 min.

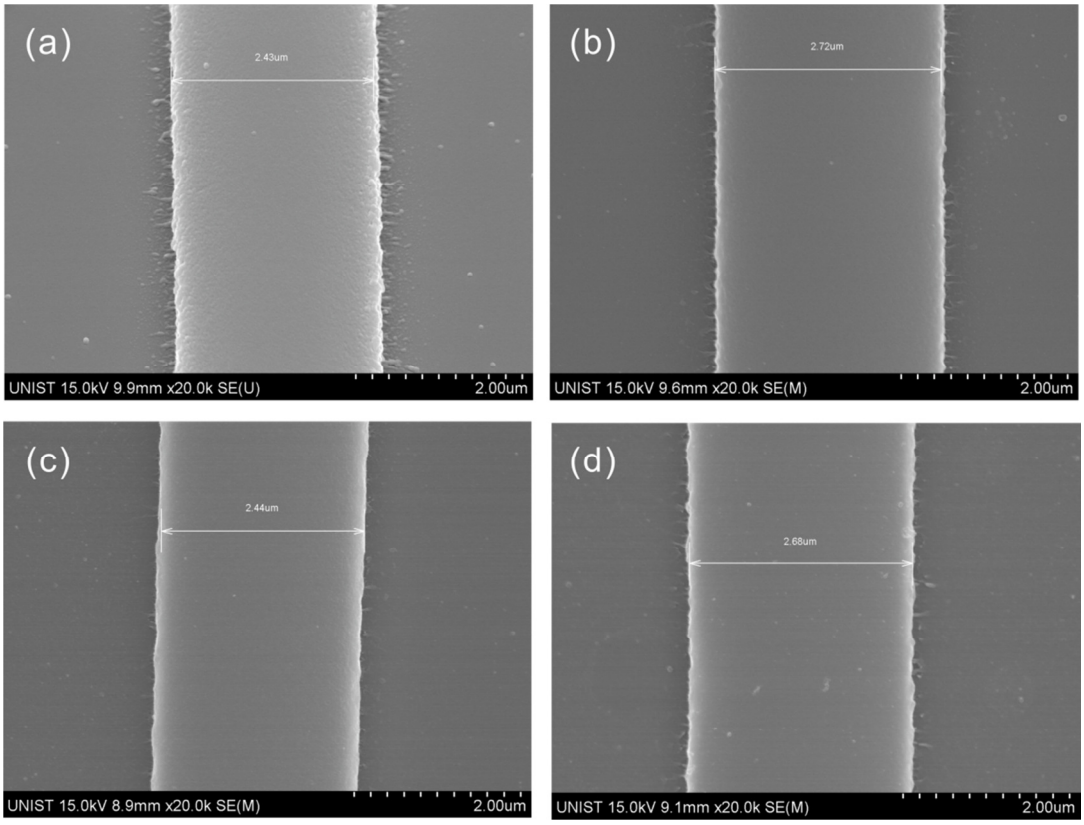

Fig. 4-3. Surface SEM images of the waveguide pattern. (a) Sample #1 (b) Sample #2 (c) Sample #3 (d) Sample #4.

All the conditions show poor side roughness. Consequently, I selected baking conditions through many experiments; soft bake : 4 minutes to 95 ℃, post bake : 1 minute to 95 ℃. Third, the width of the DLSPP waveguide pattern is determined according to the e-beam writing dose. So that also through experiments, I selected e-beam writing dose for 0.1 $\mu C/cm^2$. Fourth, the length of the waveguide pattern is long. So, stitching should not occur in e-beam lithography process. This problem is also solved through many experiments.

4.3 Fabrication Result

Fig. 4-4 (a) and (b) show SEM image of the fabricated DLSPP waveguide. According to this result, we confirmed that the DLSPP waveguide can be patterned by using either photo lithography or e-beam lithography.

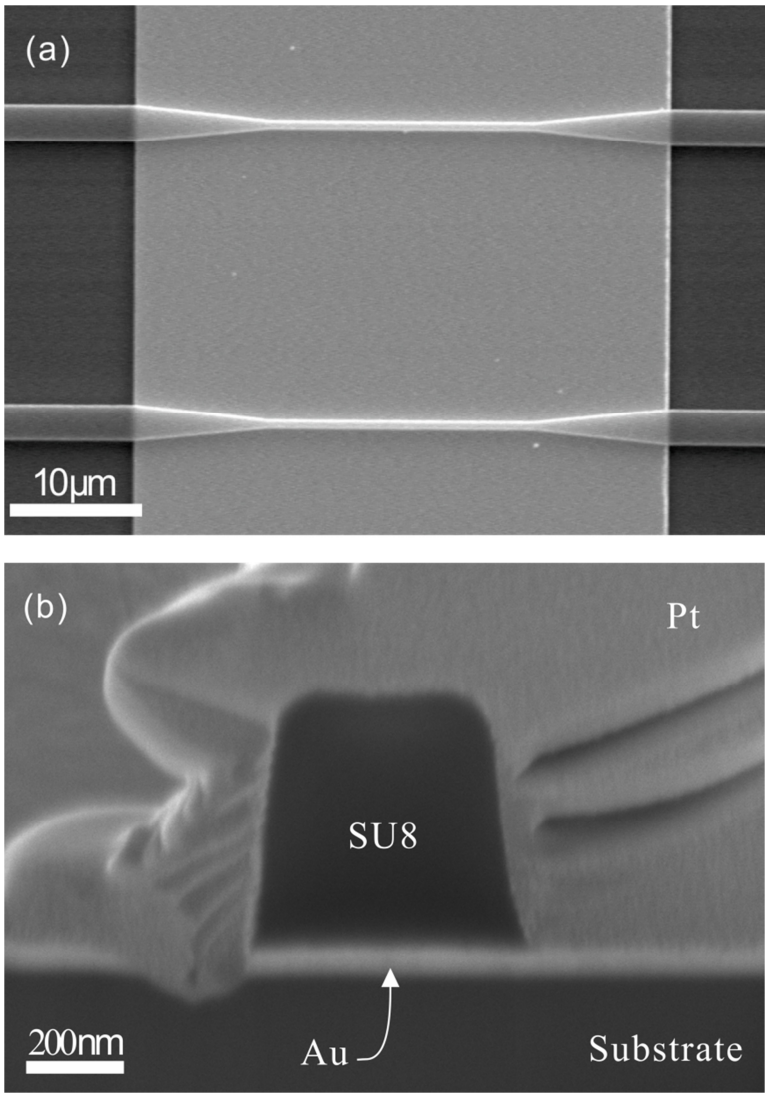

Fig. 4-4. (a) Surface SEM image of the fabricated DLSPP waveguide. (b) The cross-section image of the SU8 pattern. The SU8 pattern was covered by Pt in order to form the cross-section by using focused ion beam milling.

Chapter 6

Summary & Conclusion

In summary, First, I have investigated the two methods of improving the efficiency of the coupling between a DLSPP waveguide and a photonic waveguide and reducing the coupling region length. One method is to employ SU8, which has a refractive index larger than the previously used dielectrics, for the loaded dielectric of a DLSPP waveguide and the core of a photonic waveguide. The photonic waveguide can be coupled to the DLSPP waveguide with the minimum coupling loss of 2.3 dB through the 3-μm-long coupling region. The coupling loss and the coupling region length are smaller than those reported previously. However, the coupling region length needs to be increased up to 8 μm to make almost only the fundamental TM mode of the DLSPP waveguide excited. The other method is to modify the DLSPP waveguide into the D^2LSPP waveguide. In the D^2LSPP waveguide, HSQ and SU8 are loaded on the gold film. When the thicknesses of HSQ and SU8 are 0.4 and 0.6 μm, respectively, the photonic waveguide can be coupled to the D^2LSPP waveguide with the minimum coupling loss of 1.1 dB through the 4-μm-long coupling region. Moreover, almost only the fundamental TM mode of the D^2LSPP waveguide is excited.

A hybrid structure consisting of the photonic waveguides and the DLSPP or D^2LSPP waveguides studied in this work is expected to be useful for a highly-integrated planar lightwave circuit with a relatively low loss. A light source or a photodetector is connected to such a hybrid structure through a small-core fiber. If the small-core fiber of core diameter 1.8 μm and numerical aperture 0.35 (UHNA3, Nufern, East Granby, Conn.) is used, the loss of the butt-coupling between the fiber and the photonic waveguide is 3.1 dB. This is similar to the loss of the coupling between a single-mode fiber and the photonic waveguide in [25]. A preliminary experiment for realization of such a hybrid structure is to make a submicron SU8 pattern with an aspect ratio larger than 1.

Second, the 60° fan-shaped bend structure was proposed. The bends of DLSPP waveguides are an essential element for the implementation of various functional DLSPP waveguide devices. The 90° curved bend has 75% transmission at 4 μm bend radius. So, I have investigated the small angular bend for reducing the bend excess loss. The 60° curved bend has 81% transmission at 4.5 μm bend radius. The small angular bend has an advantage that the light can propagate smoothly. The transmission can be increased further by modifying the structure of the 60° curved bend. The 60° fan-shaped bend has 84% transmission at 2.25 μm bend radius. The fields of the mode at the inside bend are forced to propagate slowly by the fan-shaped structure. So, the fields can be propagated more smoothly. Based on this result, 60° fan-shaped bend is much more efficient than 90° curved bend. It also expected to be useful for active devices with a compact size.

Third, I fabricated these DLSPP waveguide to use standard CMOS technology. In this work, a highly-integrated planar light wave circuit with a relatively low loss may be developed and the hybrid structure may be developed soon.

REFERENCES

1. MARTIJIN, J. R. 2012. Progress in hybrid-silicon photonic integrated circuit technology. *SPIE Newsroom.*

2. LIANG, D., ROELKENS, G., BAETS, R. & BOWERS, J. E. 2010. Hybrid Integrated Platforms for Silicon Photonics. *Materials,* 3**,** 1782-1802.

3. OHTSU, M. 2009. *Nanophotonics and nanofabrication*, Wiley.

4. GRAMOTNEV, D. K. & BOZHEVOLNYI, S. I. 2010. Plasmonics beyond the diffraction limit. *Nature Photonics,* 4**,** 83-91.

5. KITTEL, C. 1996. *Introduction to Solid State Physics,* New York, Wiley.

6. BREUKELAAR, I. G. 2004. *Surface plasmon-polaritons in thin metal strips and slabs: waveguiding and mode cutoff.* B. A. Sc.Thesis, University of Ottawa.

7. RAETHER, H. 1988. *Surface Plasmons on Smooth and Rough Surfaces and on Grating,* Berlin, Springer.

8. OZBAY, E. 2006. Plasmonics: merging photonics and electronics at nanoscale dimension. *Science,* 311**,** 189-193.

9. HAN, Z., ELEZZABI, A. Y. & VAN, V. 2010. Experimental realization of subwavelength plasmonic slot waveguides on a silicon platform. *Optics Letters,* 35**,** 502-4.

10. SALAS-MONTIEL, R., APUZZO, A., DELACOUR, C., SEDAGHAT, Z., BRUYANT, A., GROSSE, P., CHELNOKOV, A., LERONDEL, G. & BLAIZE, S. 2012. Quantitative analysis and near-field observation of strong coupling between plasmonic nanogap and silicon waveguides. *Applied Physics Letters,* 100.

11. CHOO, H., KIM, M.-K., STAFFARONI, M., SEOK, T. J., BOKOR, J., CABRINI, S., SCHUCK, P. J., WU, M. C. & YABLONOVITCH, E. 2012. Nanofocusing in a metal–

insulator–metal gap plasmon waveguide with a three-dimensional linear taper. *Nature Photonics,* 6**,** 838-844.

12. KWON, M. S. 2011. Metal-insulator-silicon-insulator-metal waveguides compatible with standard CMOS technology. *Optics Express,* 19**,** 8379-8393.

13. ZHU, S. Y., LO, G. Q. & KWONG, D. L. 2012. Components for silicon plasmonic nanocircuits based on horizontal Cu-SiO2-Si-SiO2-Cu nanoplasmonic waveguides. *Optics Express,* 20**,** 5867-5881.

14. KWON, M. S., SHIN, J. S., SHIN, S. Y. & LEE, W. G. 2012. Characterization of realized metal-insulator-silicon-insulator-metal waveguides and nanochannel fabrication via insulator removal. *Optics Express,* 20**,** 21875-21887.

15. SHIN, J. S., KWON, M. S., LEE, C. H. & SHIN, S. Y. 2013. Investigation and improvement of 90° direct bends of metal-insulator-silicon-insulator-metal waveguides. *IEEE Photonics J.,* 5**,** 6601909.

16. NIELSEN, M. P., ASHFAR, A., CADIEN, K. & ELEZZABI, A. Y. 2013. Plasmonic materials for metal-insulator-semiconductor-insulator-metal nanoplasmonic waveguides on silicon-on-insulator platform. *Optics Material.,* 36**,** 294-298.

17. REINHARDT, C., PASSINGER, S., CHICHKOV, B. N., MARQUART, C., RADKO, I. P. & BOZHEVOLNYI, S. I. 2006. Laser-fabricated dielectric optical components for surface plasmon polaritons. *Optics Letters,* 31**,** 1307-1309.

18. STEINBERGER, B., HOHENAU, A., DITLBACHER, H., STEPANOV, A. L., DREZET, A., AUSSENEGG, F. R., LEITNER, A. & KRENN, J. R. 2006. Dielectric stripes on gold as surface plasmon waveguides. *Applied Physics Letters,* 88.

19. HOLMGAARD, T. & BOZHEVOLNYI, S. I. 2007. Theoretical analysis of dielectric-loaded surface plasmon-polariton waveguides. *Physical Review B,* 75.

20. ZHU, Z. H., GARCIA-ORTIZ, C. E., HAN, Z. H., RADKO, I. P. & BOZHEVOLNYI, S. I. 2013. Compact and broadband directional coupling and demultiplexing in dielectric-loaded

surface plasmon polariton waveguides based on the multimode interference effect. *Applied Physics Letters,* 103.

21. TSILIPAKOS, O., YIOULTSIS, T. V. & KRIEZIS, E. E. 2009. Theoretical analysis of thermally tunable microring resonator filters made of dielectric-loaded plasmonic waveguides. *Journal of Applied Physics,* 106.

22. GOSCINIAK, J., BOZHEVOLNYI, S. I., ANDERSEN, T. B., VOLKOV, V. S., KJELSTRUP-HANSEN, J., MARKEY, L. & DEREUX, A. 2010. Thermo-optic control of dielectric-loaded plasmonic waveguide components. *Optics Express,* 18**,** 1207-1216.

23. GOSCINIAK, J., MARKEY, L., DEREUX, A. & BOZHEVOLNYI, S. I. 2012. Efficient thermo-optically controlled Mach-Zhender interferometers using dielectric-loaded plasmonic waveguides. *Optics Express,* 20**,** 16300-16309.

24. BRIGGS, R. M., GRANDIDIER, J., BURGOS, S. P., FEIGENBAUM, E. & ATWATER, H. A. 2010. Efficient Coupling between Dielectric-Loaded Plasmonic and Silicon Photonic Waveguides. *Nano Letters,* 10**,** 4851-4857.

25. GOSCINIAK, J., VOLKOV, V. S., BOZHEVOLNYI, S. I., MARKEY, L., MASSENOT, S. & DEREUX, A. 2010b. Fiber-coupled dielectric-loaded plasmonic waveguides. *Optics Express,* 18**,** 5314-5319.

26. ANDREAS, G., JACEK, G., GONZALEZ, M. U., JAN, R., CARSTEN, R., ROMAN, K., ROMAIN, Q., BOZHEVOLNYI, S. I. & CHICHKOV, B. N. 2010. Fiber-coupled surface plasmon polariton excitation in imprinted dielectric-loaded waveguides. *International Journal of Optics***,** 897829. http://dx.doi.org/10.1155/2010/897829

27. KUDRYASHOV, V., YUAN, X. C., CHEONG, W. C. & RADHAKRISHNAN, K. 2003. Grey scale structures formation in SU-8 with e-beam and UV. *Microelectronic Engineering,* 67-8**,** 306-311.

28. DEL CAMPO, A. & GREINER, C. 2007. SU-8: a photoresist for high-aspect-ratio and 3D submicron lithography. *Journal of Micromechanics and Microengineering,* 17**,** R81-R95.

29. BÊCHE, B., PELLETIER, N., GAVOT, E. & ZYSS, J. 2004. Single-mode TE¬00-TM00 optical waveguides on SU-8 polymer. *Optics Communications,* 230**,** 91-94.

30. NEZHAD, M. P., BONDARENKO, O., KHAJAVIKHAN, M., SIMIC, A. & FAINMAN, Y. 2011. Etch-free low loss silicon waveguides using hydrogen silsesquioxane oxidation masks. *Optics Express,* 19**,** 18827-18832.

31. OULTON, R. F., BARTAL, G., PILE, D. F. P. & ZHANG, X. 2008. Confinement and propagation characteristics of subwavelength plasmonic modes. *New Journal of Physics,* 10.

32. KRASAVIN, A. V. & ZAYATS, A. V. 2008. Three-dimensional numerical modeling of photonic integration with dielectric-loaded SPP waveguides. *Physical Review B,* 78.